

Design of gate-confined quantum-dot structures in the few-electron regime

Minhan Chen and Wolfgang Porod^{a)}

Department of Electrical Engineering, University of Notre Dame, Notre Dame, Indiana 46556

(Received 13 January 1995; accepted for publication 7 March 1995)

Numerical simulations for the design of gated delta-doped AlGaAs/GaAs quantum-dot structures in the few-electron regime are presented. The confining potential is obtained from the Poisson equation with a Thomas–Fermi charge model. The electronic states in the quantum dot are then obtained from solutions of the axisymmetric Schrödinger equation. Our model takes into account the effect of surface states by viewing the exposed surface as the interface between the semiconductor and air (or vacuum). Various gate configurations and biasing modes are explored. The simulations show that the number of electrons can be effectively controlled in the few-electron regime with combined enhancement and depletion gates. © 1995 American Institute of Physics.

I. INTRODUCTION

In recent years, advanced fabrication techniques have made possible further confinement of a two-dimensional electron gas (2DEG) into wires or dots where quantum effects are significant.¹ Quantum dots have been the focus of numerous studies, and controllable loading of these dots with few electrons has been achieved,² allowing one to speak of quantum-dot hydrogen, quantum-dot helium, etc. Very recently, coupling between such close-by “quantum-dot atoms” has been demonstrated, thus realizing semiconductor “quantum-dot molecules.”³

Based on the emerging technology of quantum-dot fabrication, an application of computing with coupled quantum-dot molecules has been proposed in a series of papers.^{4,5} These so-called *quantum cellular automata* (QCA) are based on arrays of cells, each of which is composed of coupled quantum dots and occupied by few electrons. Figure 1(a) schematically shows a QCA cell consisting of five dots and occupied by two electrons. Due to the mutual Coulombic repulsion between the electrons, these cells exhibit bistable behavior which can be used to encode binary information.^{4,5} The fabrication of such a cell is a challenging problem, yet appears to be within reach of current lithographic capability.⁶ Figure 1(b) shows a possible physical realization which is based on electrostatic confinement provided by a top metallic electrode. The key implementation challenges are (i) to gain sufficient gate control in order to define quantum dots in the few-electron regime, and (ii) to place these dots sufficiently close to each other in order to make coupling possible.

In this paper, we numerically investigate the feasibility of realizing gate-controlled quantum dots in the few-electron regime for possible QCA applications. In order to achieve a crisp confining potential, we will focus on minimizing the effects of fringing fields by bringing the electrons as close as possible to the top surface. This design strategy of “trading mobility versus gate control” by utilizing near-surface 2DEGs has been pioneered by Snider *et al.*⁷ However, the resultant proximity of the quantum dot to the surface raises the question of the effect of the exposed surface on the quantum confinement. In our modeling, we explicitly include the

influence of surface states which are occupied, in a self-consistent fashion, according to the local electrostatic potential.⁸ Our modeling will show that the simple geometry of a conventional negatively biased metal electrode as shown in Fig. 1(b) does not provide sufficient gate control for QCA applications, even for extremely shallow 2DEGs. We have therefore explored the use of dual gates which, as we will demonstrate, allows one to achieve much better control of the confining potential—a result which has also been found in recent related studies.^{9,10}

There exists a large body of literature on the modeling of quantum dots; we refer to only a few representative papers.¹¹ Since the operation of such a device is primarily based on controlling the electron density by varying the confining potential, the modeling of the potential distribution and the electronic states in these structures is important. We obtain the confining potential from solutions of the axisymmetric Poisson equation with a Thomas–Fermi charge model. The electronic states in the quantum dot are subsequently determined from solutions of the axisymmetric Schrödinger equation using the previously calculated confining potential. Our simulation takes into account the effect of surface states by viewing the exposed surface as the interface between the semiconductor and the dielectric (air or vacuum). In our problem formulation, we view as the natural problem domain both the semiconductor and the dielectric.⁸ The usual Dirichlet or von Neumann boundary conditions at the exposed semiconductor surface are replaced by more physical matching conditions at the interface between the semiconductor and the dielectric. The importance of the proper choice of boundary conditions on exposed surfaces has also been stressed in Ref. 12. Fermi-level pinning is a result of our modeling, and not an input. For the numerical treatment, we have developed a combined finite-element and boundary-element method (FBEM algorithm),⁸ which is modified here for the cylindrically symmetric quantum-dot structures. We investigate the number of confined electrons and the physical size of quantum-dot structures as a function of gate geometries and biasing modes. All our modeling is performed for a temperature of 4 K.

Our modeling is aimed at exploring the parameter space for the design of quantum dots. In order to make the simulations feasible, we had to make certain simplifying assump-

^{a)}Electronic mail: Wolfgang.Porod@ND.edu

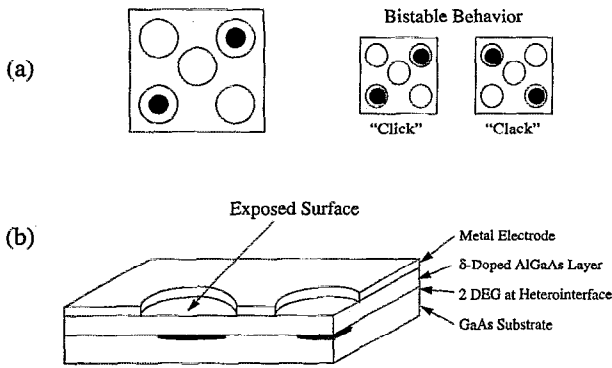


FIG. 1. (a) Schematic diagram of a bistable quantum-dot cell occupied by two electrons (see Refs. 4 and 5). (b) Physical realization by gate-controlled quantum dots.

tions. One of these assumptions is our focus on individual axially symmetric quantum dots, even though we have geometries in mind which lack this symmetry. Also, for reasons of numerical feasibility, we have chosen a Thomas–Fermi charge model in the semiconductor. Fully quantum-mechanical simulations involving the self-consistent solution of Poisson’s and Schrödinger’s equations tend to be computationally prohibitive. Also, the Thomas–Fermi charge model is known to be a reasonable approximation to a fully quantum-mechanical model.¹³ Because of the Thomas–Fermi charge model used in our calculations, the threshold voltages we predict are too low, by approximately 20 mV, due to the spacing between the bottom of the conduction band and the lowest energy level. Another issue is the treat-

ment of the impurities which may or may not be in thermal equilibrium with the semiconductor, depending upon the experimental conditions.¹⁴ In our modeling we have assumed that conditions are such that the impurities are in equilibrium with the semiconductor at the given temperature.

The remainder of this paper is organized as follows. In Sec. II, we present the problem formulation including the treatment of the exposed surface. This section outlines the generalization of our previously developed FBEM solution algorithm for Poisson’s and Schrödinger’s equations⁸ to cylindrical coordinates for the axially symmetric dot geometries. In Sec. III, we utilize the numerical calculations to discuss three different gate structures and biasing modes for the design of quantum dots in the few-electron regime. Concluding remarks are given in Sec. IV.

II. PROBLEM FORMULATION

A. Problem statement and numerical treatment

An example of a gate-confined quantum-dot structure with axial symmetry is shown in Fig. 2. In the semiconductor domain, the quantum dot is realized at the AlGaAs/GaAs heterojunction and is defined by applying an appropriate (negative) voltage V_G to the gate on the top surface. Note the opening in the gate metal which exposes the semiconductor to the dielectric (air or vacuum), as schematically shown in Fig. 2(a).

For axial symmetry, Poisson’s equation can be written in cylindrical coordinates (r, θ, z) ,

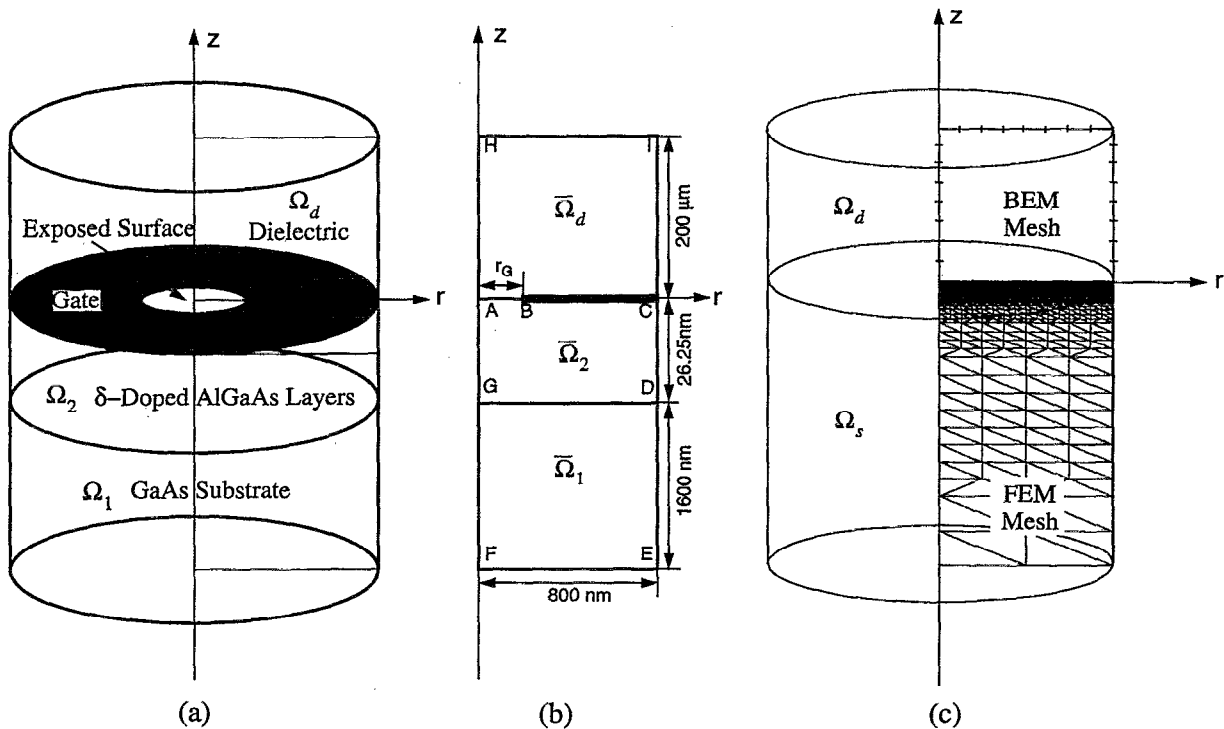


FIG. 2. Model quantum-dot structure with axial symmetry. (a) Full problem domain which consists of both the semiconductor (Ω_1 and Ω_2) and the dielectric (Ω_d) regions. (b) Two-dimensional generating areas and boundaries with typical dimensions. (c) FBEM mesh which is dense inside the semiconductor region and only consists of the discretized boundary surrounding the dielectric region.

$$\frac{1}{r} \frac{\partial}{\partial r} \left[r \epsilon \frac{\partial u(r,z)}{\partial r} \right] + \frac{\partial}{\partial z} \left[\epsilon \frac{\partial u(r,z)}{\partial z} \right] = -f[u(r,z)], \quad (1)$$

where the electrostatic potential ϕ is contained in the reduced variable $u = (E_C(\phi) - E_F)/kT$ which measures the separation between the conduction-band edge and the Fermi energy in units of the thermal energy kT , and ϵ is the dielectric constant. The right-hand-side term represents the charge density in the semiconductor, with $f = e^2(p - n + N_D^+ - N_A^-)/kT$ and all symbols have their conventional meaning. A semiclassical Thomas–Fermi charge model is assumed for the equilibrium electron and hole densities which are given by a Fermi–Dirac integral of order 1/2.^{8,15}

In order to solve Eq. (1), we utilize our previously developed FBEM algorithm,⁸ which is a combined finite element method (FEM)¹⁶ for the semiconductor domain and a boundary element method¹⁷ for the dielectric region. The generating domains and boundaries are shown in Fig. 2(b), and the FBEM mesh is shown in Fig. 2(c). In its original form, the FBEM algorithm was developed for Cartesian coordinates, and we generalize it here for cylindrical coordinates. We will briefly describe the FBEM algorithm below and refer the reader to Ref. 8 for further details.

For the semiconductor domain Ω_s , with $\Omega_s = \Omega_1 \cup \Omega_2$, the standard FEM discretization of Eq. (1) results in the following nonlinear system of equations:

$$\begin{aligned} \mathbf{K}_{11} \mathbf{u}_0^s + \mathbf{K}_{12} \mathbf{u}_{BA}^s &= \mathbf{P}_f^s, \\ \mathbf{K}_{12}^T \mathbf{u}_0^s + \mathbf{K}_{22} \mathbf{u}_{BA}^s &= \mathbf{P}_{BA}^s, \end{aligned} \quad (2)$$

where \mathbf{u}_{BA}^s and \mathbf{P}_{BA}^s contain the potentials and nodal forces at the nodes on the interface $\partial\Omega_{BA}$ between the semiconductor and the dielectric, whereas \mathbf{u}_0^s and \mathbf{P}_f^s contain the potential and nodal forces at all other nodes inside the semiconductor domain, and \mathbf{K} is the stiffness matrix.

The dielectric domain Ω_d is a charge-free region. The governing equation is Laplace's equation. Since the fundamental solution of Laplace's equation is known, a boundary integral equation technique can be employed. With the known three-dimensional fundamental solution of Laplace's equation in cylindrical coordinates and its associated dielectric flux density, the boundary contour $\partial\Omega_d$ can be calculated explicitly in terms of complete elliptic integrals of the first and second kind, $K(m)$ and $E(m)$, respectively.^{17,18} The resultant system of equations can be expressed as

$$\begin{aligned} \mathbf{S}_{11} \mathbf{u}_0^d + \mathbf{S}_{12} \mathbf{u}_{BA}^d &= \mathbf{P}_0^d, \\ \mathbf{S}_{21} \mathbf{u}_0^d + \mathbf{S}_{22} \mathbf{u}_{BA}^d &= \mathbf{P}_{BA}^d, \end{aligned} \quad (3)$$

where \mathbf{S} is the equivalent stiffness matrix and \mathbf{P}^d is the equivalent nodal force vector.

The matching conditions at the exposed surface are given in discretized form by⁸

$$\mathbf{u}_{BA}^s = \mathbf{u}_{BA}^d = \mathbf{u}_{BA}, \quad (4)$$

$$\mathbf{P}_{BA}^s + \mathbf{P}_{BA}^d = \frac{e}{kT} \mathbf{Q}_{\text{int}}, \quad (5)$$

where $\mathbf{Q}_{\text{int}} = \mathbf{Q}_{\text{int}}(\mathbf{u}_{BA})$ is the nodal charge density on the exposed semiconductor surface.

A global system of equations is formed by coupling the semiconductor, Eq. (2), to the dielectric, Eq. (3), while enforcing the matching conditions, Eqs. (4) and (5),

$$\begin{pmatrix} \mathbf{S}_{11} & \mathbf{S}_{12} & \mathbf{0} & \mathbf{0} \\ \mathbf{S}_{21} & \mathbf{S}_{22} & \mathbf{0} & \mathbf{I} \\ \mathbf{0} & \mathbf{K}_{12} & \mathbf{K}_{11} & \mathbf{0} \\ \mathbf{0} & \mathbf{K}_{22} & \mathbf{K}_{12}^T & -\mathbf{I} \end{pmatrix} \begin{pmatrix} \mathbf{u}_0^d \\ \mathbf{u}_{BA}^d \\ \mathbf{u}_0^s \\ \mathbf{P}_{BA}^s \end{pmatrix} = \begin{pmatrix} \mathbf{P}_0^d \\ \mathbf{Q}_{\text{int}} \\ \mathbf{P}_f^s \\ \mathbf{0} \end{pmatrix}. \quad (6)$$

Solution of this set yields the potential distribution in the semiconductor and dielectric domains, including the interface $\partial\Omega_{BA}$, and the nodal flux on $\partial\Omega_{BA}$.

The confined electronic quantum-dot states at the AlGaAs/GaAs interface are obtained by solving the axisymmetric Schrödinger equation for a computed axially symmetric potential profile $V(r,z)$,

$$\psi_l = g_l(r,z) e^{il\theta}, \quad (7)$$

$$\begin{aligned} -\frac{\hbar^2}{2m^*} \left[\frac{1}{r} \frac{\partial}{\partial r} \left(r \frac{\partial}{\partial r} \right) + \frac{\partial^2}{\partial z^2} \right] g_l(r,z) \\ + \left[V(r,z) + \frac{\hbar^2 l^2}{2m^* r^2} \right] g_l(r,z) = E_l g_l(r,z). \end{aligned} \quad (8)$$

ψ_l is the electronic wave function which may be factored due to the axial symmetry; $\exp(il\theta)$ is the angular momentum part and g_l is a function of only (r,z) . $V(r,z) = kTu(r,z)$ is the axisymmetric confining potential and m^* denotes the effective mass.

The asymptotic decay of the wave function far from the dot region provides zero-valued Dirichlet and/or Neumann boundary conditions. Standard FEM discretization of Eq. (8) results in the following linear eigenvalue problem:

$$\mathbf{A} \mathbf{g}_l = E_l \mathbf{B} \mathbf{g}_l, \quad (9)$$

where \mathbf{g}_l is the vector of nodal values for the axisymmetric wave functions on the (r,z) plane, and E_l is the eigenenergy. Since we are interested in only the lowest few eigenstates, Eq. (9) is solved by a subspace iteration method.^{15,16} The electronic wave functions ψ_l can then be obtained directly from Eq. (7).

B. Interface charge density on the exposed semiconductor surface

In order to solve the above problem, the interface charge density Q_{int} must be given in order to specify the matching condition (5) on the exposed semiconductor surface. It is well known that energy states lying within the band gap play a dominant role for the interface charge Q_{int} on semiconductor surfaces.^{19–22}

In this paper, the surface states are assumed to possess acceptor- and donorlike characteristics,²¹ with densities D_A^s and D_D^s , respectively. The semiconductor surface charge density as a function of the surface potential u_{BA} is given by Fermi–Dirac statistics with an appropriate quasi-Fermi level E_F^s for cases of applied bias²⁰

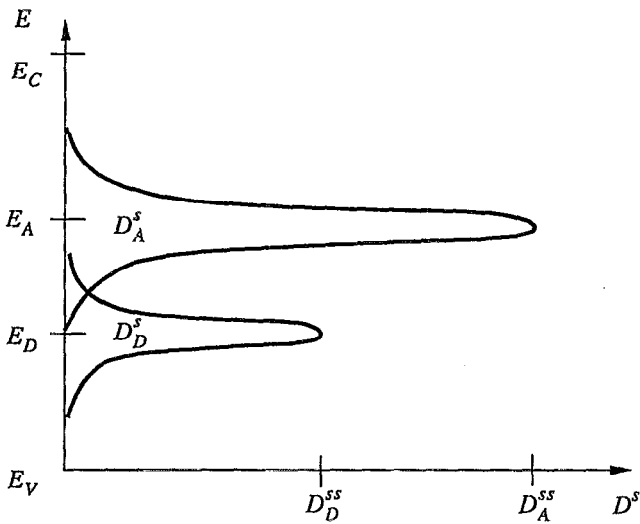


FIG. 3. Typical Gaussian energy distribution of interface states in the semiconductor band gap.

$$Q_{\text{int}}(u_{BA}) = -e \int_{E_V}^{E_C} \frac{D_A^s}{1 + \exp[(E - E_F^s)/kT]} dE + e \int_{E_V}^{E_C} \frac{D_D^s \exp[(E - E_F^s)/kT]}{1 + \exp[(E - E_F^s)/kT]} dE. \quad (10)$$

As schematically shown in Fig. 3, typical Gaussian energy distributions are assumed for the surface states

$$D_A^s = D_A^{ss} \exp\left(-\frac{(E - E_A)^2}{2\Delta E_A^2}\right), \quad (11)$$

$$D_D^s = D_D^{ss} \exp\left(-\frac{(E - E_D)^2}{2\Delta E_D^2}\right). \quad (12)$$

The acceptor- (donor-) like surface-state densities are characterized by their height D_A^{ss} (D_D^{ss}), centroid E_A (E_D), and width ΔE_A (ΔE_D).

In our surface charge model, following Ref. 21, the acceptor- and donorlike states are assumed to be centered around energies $E_A = 0.75$ eV and $E_D = 0.5$ eV, respectively,

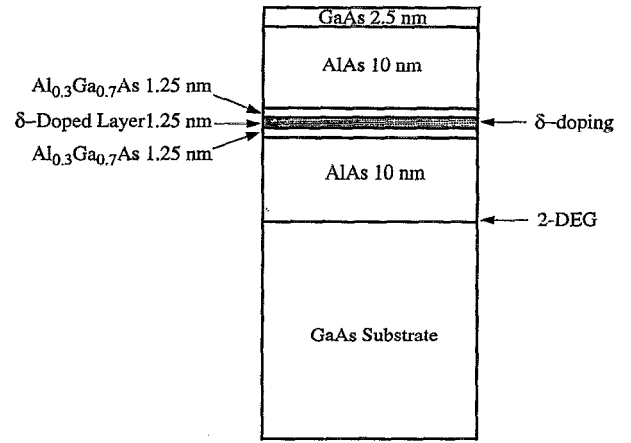


FIG. 4. Schematic diagram of the delta-doped shallow 2DEG structure utilized here (after Ref. 26).

measured from the valence-band edge. In the available literature, there are no unique agreed-upon values for the heights and the widths of the distributions, but there is general agreement on the range of the parameters. Here, we assume equal values for the acceptor- and donorlike surface-state density peaks $D_A^{ss} = D_D^{ss} = 6 \times 10^{14} \text{ cm}^{-2} \text{ eV}^{-1}$ and widths $\Delta E_D = \Delta E_A = 0.1$ eV. With this choice of parameter values, we are able to reproduce the observed Fermi-level pinning behavior.¹⁹⁻²² In the above choice of the parameter values, the location of the charge centroids is critical. Less critical are the peak heights and widths, which may be varied over the range of values reported in the literature,¹⁹⁻²² while still yielding Fermi-level pinning behavior. These issues pertaining to the choice of the surface-state charge model will be discussed in greater detail elsewhere.²³

The strong nonlinearity of the interface charge as a function of the band bending at the surface may cause numerical convergence problems, particularly for low temperatures. We implemented a modified Bank-Rose damping scheme to stabilize the convergence by adaptive underrelaxation and to accelerate the convergence speed of Newton's method.^{24,25} The combination of our coupled axisymmetric finite-

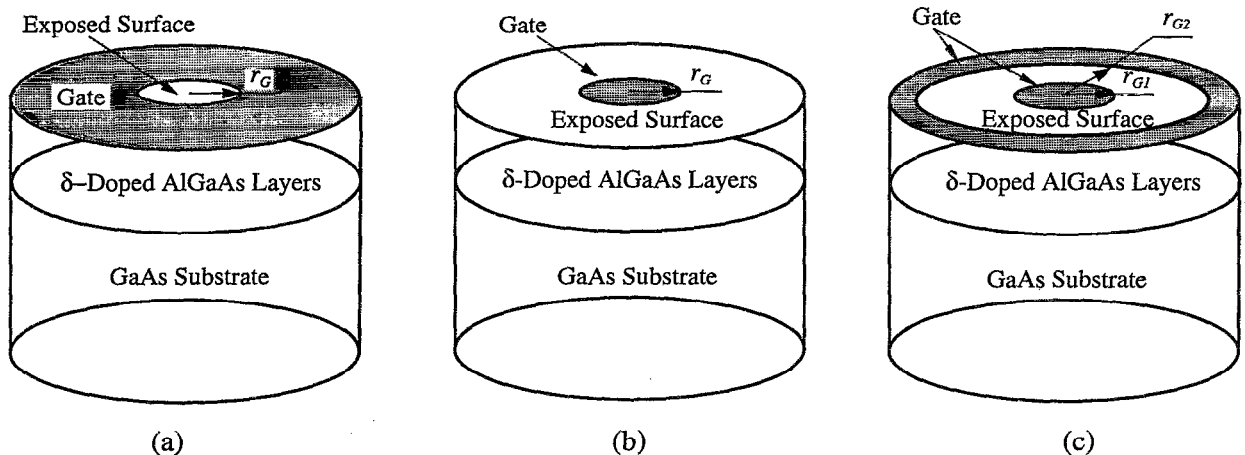


FIG. 5. Three types of top gate structures with axial symmetry: (a) depletion gate, (b) enhancement gate, and (c) combined enhancement/depletion gates.

element/boundary-element algorithm and the adaptive damping scheme was found to perform quite satisfactorily.

III. QUANTUM-DOT DESIGN

The results shown in this section concentrate on the design of quantum dots in the few-electron regime for possible applications in QCA.^{4,5} Our simulations are based on the delta-doped AlGaAs/GaAs structure reported in Ref. 26, where it was shown that sheet carrier concentrations of $3.4 \times 10^{11} \text{ cm}^{-2}$ and Hall mobilities of $1.2 \times 10^6 \text{ cm}^2 \text{ V}^{-1} \text{ s}^{-1}$ at 4 K may be achieved with a shallow 2DEG 25 nm below the semiconductor/vacuum interface. Figure 4 shows the layer structure utilized in our modeling below.

We will explore three types of axially symmetric top gate geometries, which are schematically shown in Fig. 5. The conventional biasing mode is one where a negative bias is applied to the gate, thus depleting the 2DEG underneath the metal electrode; we will refer to this mode as “depletion mode” biasing. As shown in Fig. 5(a), a quantum dot may be realized below the circular hole in the negatively biased gate. One may also utilize structures with an initially depleted 2DEG, e.g., by surface depletion due to Fermi-level pinning. An electron density may then be induced underneath a positively biased gate. This so-called “enhancement mode” biasing is schematically shown in Fig. 5(b). By combining the above two mechanisms, we designed a third type of quantum-dot structure with combined center enhancement and surrounding depletion gates, as shown in Fig. 5(c). We will demonstrate that the dot occupation in this combined enhancement/depletion mode can be accurately controlled by adjusting the positive and/or negative bias on the gates.

A. Depletion gates

The n -type sheet doping concentration for the delta-doped AlGaAs layer is assumed to be $5.0 \times 10^{12} \text{ cm}^{-2}$ which leads to the formation of a 2DEG along the AlAs/GaAs heterointerface without gate bias. By applying a sufficiently negative bias to the top gate shown in Fig. 5(a), a quantum dot may be realized. For typical parameter values, the resulting potential variations inside the semiconductor are plotted in Fig. 6, (a) perpendicular and (b) parallel to the surface. Figure 6(a) shows a plot of the conduction-band profile perpendicular to the semiconductor surface at the center of the circular gate opening. Electrons accumulate at the GaAs-substrate/AlAs interface, where the conduction-band edge dips below the Fermi level which is taken as the zero of the energy scale. Care has to be taken that no parallel conducting layer forms in the dopant plane. Figure 6(b) is a plot of the conduction-band edge parallel to the heterointerface (on the GaAs side), which shows the quantum-dot confining potential. Again, electron accumulation occurs in the region where the conduction band dips below the semiclassical Fermi level indicated by an arrow. The physical size of the quantum dot can be measured as the radius of the circular cross section of the conduction band at the Fermi level, which we will call the “physical dot radius” r_{dot} . Device applications of such a structure are based on the ability to utilize the gate bias and the gate size to modulate both the number of the confined electrons and the physical size of the quantum dots.

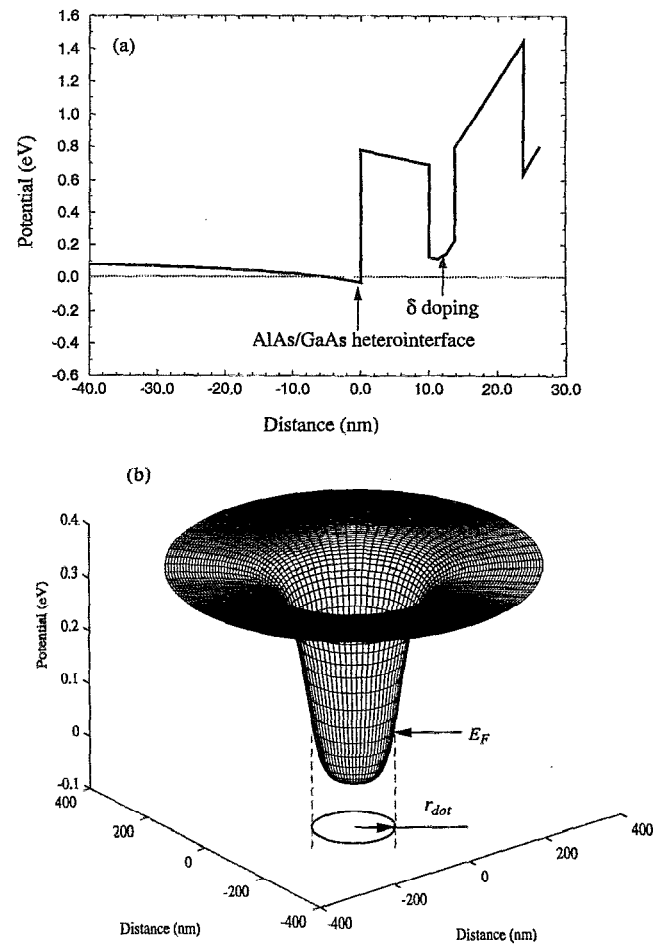


FIG. 6. Typical quantum-dot potential profile where the Fermi level E_F and the physical dot radius r_{dot} are indicated: (a) perpendicular to the semiconductor surface at the center of the dot, (b) parallel to the substrate GaAs/AlAs heterointerface (on the GaAs side).

Figure 7 shows the size and occupation of quantum dots for depletion mode biasing. The radius of quantum dots, r_{dot} , induced by three different sizes of metal-electrode openings, r_G , is plotted in Fig. 7(a) as a function of the (negative) gate bias voltage. As expected, the dot radius decreases with increasing gate bias. Eventually, the dot is completely depleted at a certain threshold voltage, which depends upon the gate geometry. Figure 7(b) shows the corresponding number of electrons in each dot, which is obtained by integrating the electron density over the dot region. We see that the occupation number sensitively depends upon the gate bias, and that the few-electron regime may be realized for reasonable values of gate dimensions and bias voltages. As an example, for a 50-nm-radius metal-gate opening, the few-electron regime is reached for a (negative) bias greater than 0.5 V; however, for a bias greater than a threshold of 0.53 V, the dot is totally depleted.

Note that the confining potential is rather gradual (perhaps surprisingly so). In order to achieve a dot radius of, say, 10 nm, the radius of the gate opening has to be at least 30 nm. Even though we are utilizing here a 2DEG which is extremely close to the surface, the features in the plane of the

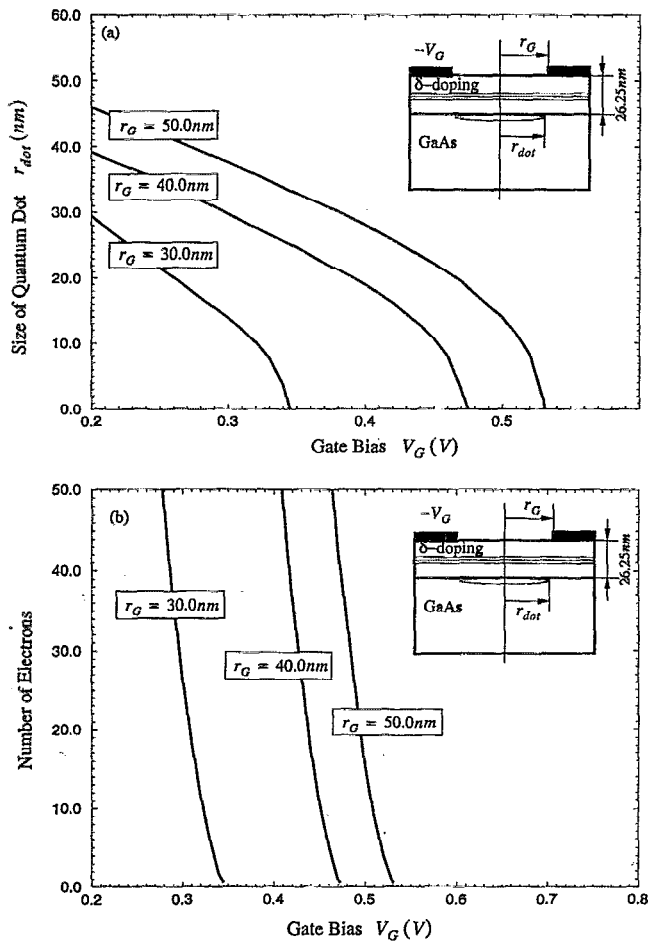


FIG. 7. Size and occupation of quantum dots for depletion mode biasing. (a) Radius of quantum dots, r_{dot} , induced for three different sizes of metal-electrode openings, r_G , as a function of the (negative) gate bias voltage; (b) corresponding number of electrons in each dot.

electrons are a factor of 3 (or more) smaller than the features of the surface gates. As a consequence, it is not possible to place dots (in the 2DEG plane) close to each other (since they cannot be closer than the corresponding openings in the metal electrode). We conclude that depletion mode biasing is not a promising candidate for QCA applications.

B. Enhancement gates

The n -type sheet doping concentration for the delta-doped AlGaAs layer is now assumed to be $3.0 \times 10^{12} \text{ cm}^{-2}$ which leads to a normally depleted 2DEG. Without an applied gate bias, the conduction-band edge along the GaAs/AlAs heterointerface is close *and* above the Fermi level due to the effect of the pinned GaAs surface potential. By applying a small positive bias on the center circular gate, shown in Fig. 5(b), quasi-zero-dimensional electronic states may be induced underneath the top electrode.

Figure 8 shows the size and occupation of quantum dots for enhancement mode biasing. The radius of quantum dots, r_{dot} , induced by three different sizes of metal electrodes, r_G , is plotted in Fig. 8(a) as a function of the (positive) gate bias voltage. Again, Fig. 8(b) shows the corresponding number of

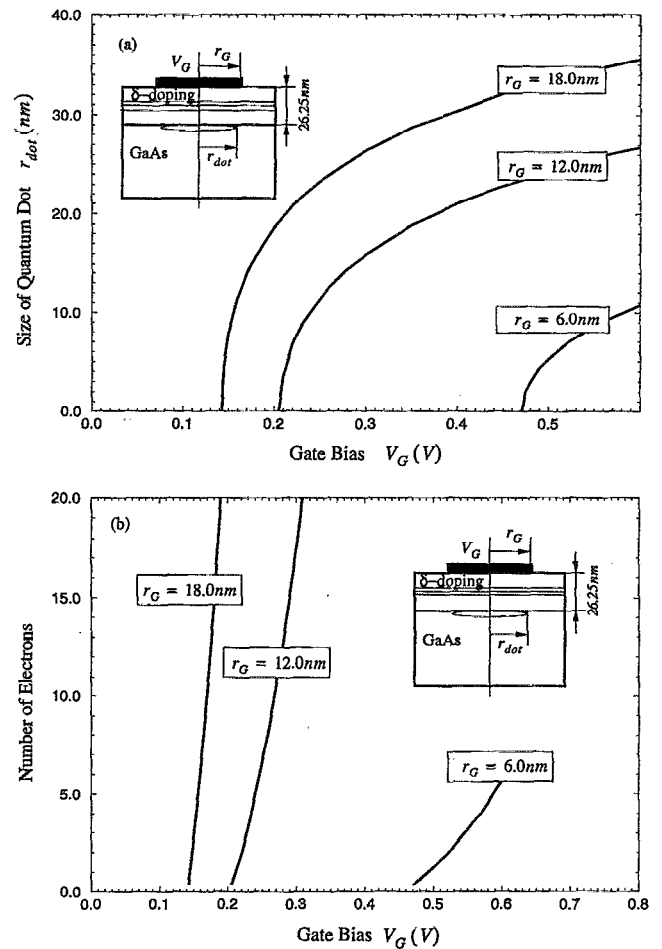


FIG. 8. Size and occupation of quantum dots for enhancement mode biasing. (a) Radius of quantum dots, r_{dot} , induced for three different sizes of metal electrodes, r_G , as a function of the (positive) gate bias voltage; (b) corresponding number of electrons in each dot.

electrons in each dot. For larger gate biases, both the radius and the occupation of each dot increases. For example, for a circular enhancement gate with 12 nm radius, the threshold voltage is about 0.2 V and, in the few-electron regime, an additional electron is added for every 10 mV increment in the gate bias.

The control of the threshold voltage in this mode is critical. The gate bias cannot be too large since the structure becomes leaky due to tunneling between the 2DEG and the metal electrode. Another problem at positive biasing is that parasitic electron accumulation occurs in the delta-doped layers, as may be seen from Fig. 6(a).

We see that in this mode, the induced quantum dot (in the plane of the electrons) may be similar in size to the top metal electrode. QCA applications appear to be feasible, since it is possible to realize arrangements of quantum dots which are *both* close together *and* occupied by few electrons.

C. Combined enhancement/depletion gates

We will now demonstrate that a combination of enhancement and depletion gates, schematically shown in Fig. 5(c), provides effective control of the threshold voltage. The main

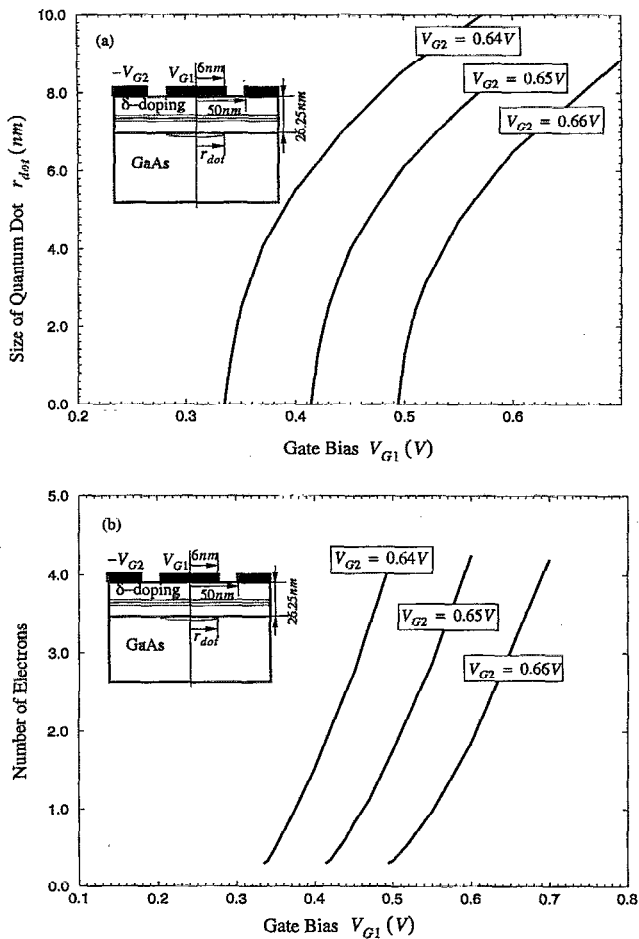


FIG. 9. Size and occupation of quantum dots for combined enhancement/depletion mode biasing. The gate dimensions are indicated in the insets. (a) Radius of quantum dots, r_{dot} , induced by three different voltages on the depletion gate V_{G2} as a function of the enhancement gate bias voltage V_{G1} . (b) Corresponding number of electrons in each dot.

idea is to negatively bias the outer gates (gate 2) such that the electron density is depleted or near depletion; a positive bias on the inner gate (gate 1) is then utilized to induce the dot and to control its occupation.

Figure 9 shows an example of the size and occupation of quantum dots for combined enhancement/depletion mode biasing. The n -type sheet doping concentration for the delta-doped AlGaAs layer is assumed to be $3.0 \times 10^{12} \text{ cm}^{-2}$, which is the same as for the above enhancement gate structure. In this example, we have chosen a radius of $r_{G1} = 6 \text{ nm}$ for the center enhancement gate, and a radius of $r_{G2} = 50 \text{ nm}$ for the surrounding depletion gate. The radius of quantum dots, r_{dot} , induced by three different voltages on the depletion gate V_{G2} is plotted in Fig. 9(a) as a function of the enhancement gate bias voltage V_{G1} . Figure 9(b) shows the corresponding number of electrons in each dot. We see that variations of the depletion gate bias of 10 mV will result in threshold-voltage variations of as much as 80 mV. This biasing mode appears to be an effective way of controlling the quantum-dot threshold voltage in the few-electron regime.

Note that the curves in Fig. 9(b) are much less steep than the corresponding ones in Figs. 8(b) and 7(b). This means

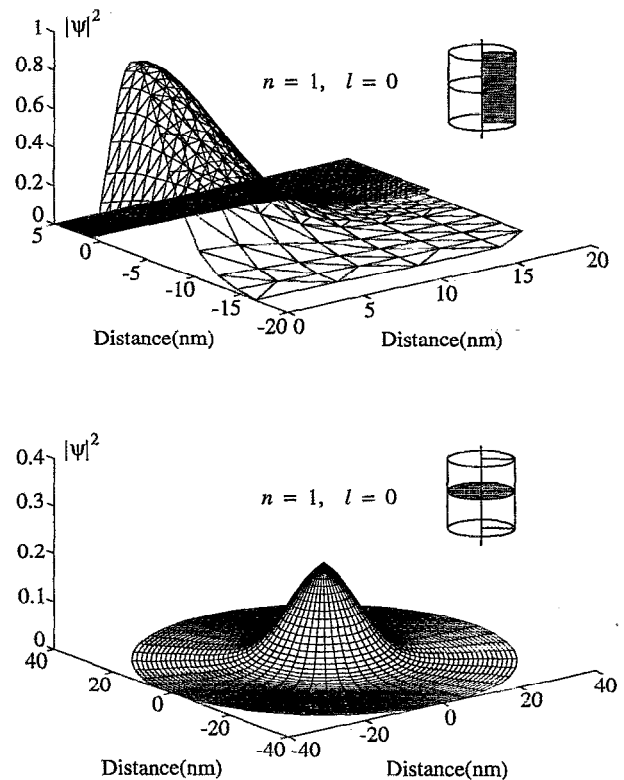


FIG. 10. Typical lowest energy wave function. As schematically shown in the insets, the upper panel is a plot in the (r, z) plane, and the lower panel in the (r, θ) plane at the GaAs/AlAs heterointerface.

that the combined enhancement/depletion mode allows more effective gate control of the quantum-dot occupation than either the enhancement or depletion modes alone.

Several enhancement gates may be placed inside the same depletion gate opening. In particular, one depletion gate may define a single QCA cell and each dot is realized by separate enhancement gates. Work on utilizing this design strategy to realized QCA is in progress.

D. Quantized electronic states

The quantum-dot structures support three-dimensionally confined electronic states. The separation of the quantized energy levels is also of interest for applications. To this end, we have solved the axisymmetric Schrödinger equation, Eqs. (7) and (8), for a given confining potential.

Figures 10 and 11 show a typical example of the wave functions for the first and second electronic states, respectively. The wave function of the lowest energy state is plotted in the upper panel of Fig. 10 in the (r, z) plane and in the lower panel in the (r, θ) plane, as schematically indicated in the insets. The corresponding plots of the wave function of the second-lowest energy state are shown in Fig. 11. The energy separation in this example (enhancement gate structure with a 20 nm radius) is $E_2 - E_1 = 13 \text{ meV}$.

IV. CONCLUSION

We have presented our numerical simulations for the design of gated delta-doped AlGaAs/GaAs quantum-dot struc-

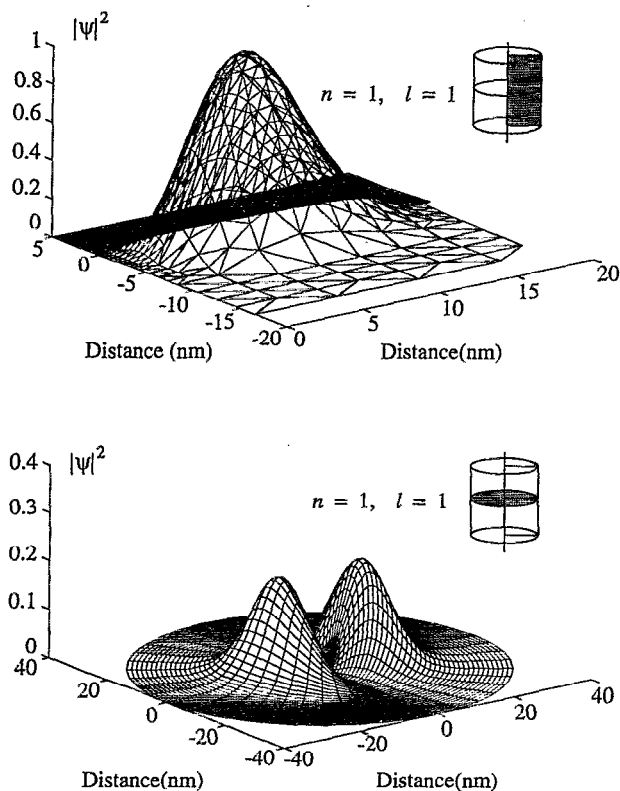


FIG. 11. Typical second-lowest energy wave function. As schematically shown in the insets, the upper panel is a plot in the (r, z) plane, and the lower panel in the (r, θ) plane at the GaAs/AlAs heterointerface.

tures in the few-electron regime. The confining potential is obtained from the axisymmetric Poisson equation with a semiclassical Thomas–Fermi charge model. The electronic states in the quantum dot are subsequently determined from solutions of the axisymmetric Schrödinger equation using the previously calculated confining potential. Our simulation takes into account the effect of surface states by viewing the exposed surface as the interface between the semiconductor and the dielectric (air or vacuum). For the numerical treatment, we have developed a combined finite-element and boundary-element method (FBEM algorithm).

Utilizing a realistic material system with a shallow 2DEG, we have demonstrated that it is possible to realize quantum-dot structures in the few-electron regime. Our results indicate that the most promising design strategy is to utilize combined enhancement/depletion gates, which allow effective control of the threshold voltage. These structures appear to be promising candidates for future QCA applications.

ACKNOWLEDGMENTS

The authors wish to thank Greg Bazán, Dr. Gary H. Bernstein, Dr. Henry K. Harbury, Dr. David J. Kirkner, Dr.

Craig S. Lent, Xinhui Niu, Dr. Zhian Shao, Dr. R. Kent Smith, and Dr. Gregory L. Snider for numerous helpful discussions and suggestions. This work was supported in part by AFOSR and ARPA/ONR.

- ¹ *Nanostructures and Mesoscopic Systems*, edited by W. P. Kirk and M. A. Reed (Academic, Boston, 1992).
- ² Ch. Sikorski and U. Merkt, *Phys. Rev. Lett.* **62**, 2164 (1989); J. Alsmeyer, E. Batke, and J. P. Kotthaus, *Phys. Rev. B* **41**, 1699 (1990); B. Meurer, D. Heitman, and K. Ploog, *Phys. Rev. Lett.* **68**, 1371 (1992); R. C. Ashoori, H. L. Störmer, J. S. Weiner, L. N. Pfeiffer, K. W. Baldwin, and K. W. West, *ibid.* **71**, 613 (1993); H. Drexler, D. Leonard, W. Hansen, J. P. Kotthaus, and P. M. Petroff, *ibid.* **73**, 2252 (1994).
- ³ M. Kemerink and L. W. Molenkamp, *Appl. Phys. Lett.* **65**, 1012 (1994); S. W. Hwang, B. D. Yu, T. Sakamoto, and K. Nakamura, *Superlatt. Microstruct.* (in press); F. Hofmann, T. Heinzel, D. A. Wharam, J. P. Kotthaus, G. Böhm, W. Klein, G. Tränkle, and G. Weimann (preprint, 1995).
- ⁴ C. S. Lent, P. D. Tougaw, W. Porod, and G. H. Bernstein, *Nanotechnology* **4**, 49 (1993).
- ⁵ C. S. Lent, P. D. Tougaw, and W. Porod, *Appl. Phys. Lett.* **62**, 714 (1993); P. D. Tougaw, C. S. Lent, and W. Porod, *J. Appl. Phys.* **74**, 3558 (1993).
- ⁶ X. Huang, G. Bazán, and G. H. Bernstein, *J. Vac. Sci. Technol. B* **11**, 2565 (1993).
- ⁷ G. L. Snider, M. S. Miller, M. J. Rooks, and E. L. Hu, *Appl. Phys. Lett.* **59**, 2727 (1991); G. L. Snider, I.-H. Tan, and E. L. Hu, *J. Appl. Phys.* **68**, 5922 (1990).
- ⁸ M. Chen, W. Porod, and D. J. Kirkner, *J. Appl. Phys.* **75**, 2545 (1994).
- ⁹ Y. Wang and S. Y. Chou, *Appl. Phys. Lett.* **63**, 2257 (1993); **64**, 309 (1994); **65**, 2072 (1994).
- ¹⁰ J. P. Lu, X. Ying, and M. Shayegan, *Appl. Phys. Lett.* **65**, 2320 (1994).
- ¹¹ A. Kumar, S. E. Laux, and F. Stern, *Phys. Rev. B* **42**, 5166 (1990); D. Pfannkuche and R. R. Gerhardt, *Phys. Rev. B* **44**, 13132 (1991); M. Macucci, K. Hess, and G. J. Iafrate, *ibid.* **48**, 17354 (1993); M. Stopa, *ibid.* **48**, 18340 (1993).
- ¹² J. H. Davies and I. A. Larkin, *Phys. Rev. B* **49**, 4800 (1994).
- ¹³ J. H. Luscombe, *Nanotechnology* **4**, 1 (1993).
- ¹⁴ A. Kumar, S. E. Laux, F. Stern, A. Zaslavsky, J. M. Hong, and T. P. Smith, III, *Phys. Rev. B* **48**, 4899 (1993).
- ¹⁵ W. Porod, H. K. Harbury, and S. M. Goodnick, *Appl. Phys. Lett.* **61**, 1823 (1992); H. K. Harbury, W. Porod, and S. M. Goodnick, *J. Appl. Phys.* **73**, 1509 (1993).
- ¹⁶ K. J. Bathe, *Finite Element Procedures in Engineering Analysis* (Prentice-Hall, Englewood Cliffs, NJ, 1982).
- ¹⁷ C. A. Brebbia, J. C. F. Telles, and L. C. Wrobel, *Boundary Element Techniques* (Springer, Berlin, 1984).
- ¹⁸ *Handbook of Mathematical Functions with Formulas, Graphs, and Mathematical Tables*, edited by M. Abramowitz and I. A. Stegun (Dover, New York, 1965).
- ¹⁹ E. H. Rhoderick and R. H. Williams, *Metal–Semiconductor Contacts* (Oxford University, New York, 1988).
- ²⁰ A. M. Cowley and S. M. Sze, *J. Appl. Phys.* **36**, 3212 (1965).
- ²¹ W. E. Spicer, I. Lindau, P. Skeath, and C. Y. Su, *J. Vac. Sci. Technol.* **17**, 1019 (1980).
- ²² W. Mönch, *Surf. Sci.* **132**, 92 (1983).
- ²³ M. Chen and W. Porod (unpublished).
- ²⁴ R. E. Bank and D. J. Rose, *SIAM J. Numer. Anal.* **17**, 806 (1980).
- ²⁵ D. Kincaid and W. Cheney, *Numerical Analysis* (Brooks/Cole, Belmont, 1991).
- ²⁶ J. E. F. Frost, D. A. Ritchie, and G. A. C. Jones, *J. Cryst. Growth* **111**, 305 (1991).

Journal of Applied Physics is copyrighted by the American Institute of Physics (AIP). Redistribution of journal material is subject to the AIP online journal license and/or AIP copyright. For more information, see <http://ojps.aip.org/japo/japcr/jsp>
Copyright of Journal of Applied Physics is the property of American Institute of Physics and its content may not be copied or emailed to multiple sites or posted to a listserv without the copyright holder's express written permission. However, users may print, download, or email articles for individual use.